



Flexible 3D porous boron nitride interconnected network as a high-performance Li-and Na-ion battery electrodes

Nabil Khossossi^a, Deobrat Singh^a, Wei Luo^a, Rajeev Ahuja^{*,a,b}

^a Condensed Matter Theory Group, Materials Theory Division, Department of Physics and Astronomy, Uppsala University, Box 516, Uppsala 75120, Sweden

^b Department of Physics, Indian Institute of Technology Ropar, Rupnagar 140001, Punjab, India

ARTICLE INFO

Keywords:

Electrochemical energy storage
3D porous boron nitride
Zigzag BN nanoribbons
Iz1-BN
Lithium ion battery
Sodium ion battery density-functional calculations

ABSTRACT

To achieve the high-rate efficiency in a electrochemical energy storage technologies, it is vital for the battery anode to be electronically as well as ionically conductive. Such a requirement has boosted the survey of three-dimensional (3D) porous networks made up of light-weight non-metallic elements, like carbon, boron, and nitride. A wide range of 3D porous materials composed of carbon and/or boron for Li/Na-ion batteries have been recently reported, whereas analogous efforts for lightest 3D porous boron nitride are yet to be addressed. In this work, we explore the 3D porous boron nitride network namely sp^3 -linked zigzag BN nanoribbons (BNNRs) with a width of 1 (Iz1-BN) by assembling the 2D zigzag BNNRs and its first ever application as battery anodes for Li and Na ion batteries. Upon a consistent DFT and AIMD computations, It is revealed that the 3D porous Iz1-BN material is chemically and thermally stable and yields a high specific capacity of about 539.94 mAh/g with respect to the commercialized graphite (372 mAh/g for LIBs) and recently reported Janus-graphite anode (≈ 332 mAh/g for SIBs), fast (Li^+, Na^+)-ionic diffusion, low potential voltage, and slight volume-expansion. Such puzzling electrochemical characteristics, along with the light-weight and high abundance of B and N elements, strongly support the possibility of 3D porous BN as a desirable candidate for Li and Na-ion battery anodes.

1. Introduction

Over the past few decades, the energy related considerations have received tremendous scrutiny as a result of the ever-increasing energy consumption from self powered electronic systems to the electric/hybrid-driven vehicles and other high-tech applications such as the large scale energy storage and so on[1–3]. Since then, to meet such ever-growing energy demand, rechargeable batteries based on either lithium-ion or sodium-ion have been widely probed through both experimental and computational approaches[4–6]. In spite of their promise as a new chemistry, Li-ion batteries (LIBs) remain plagued by a number of limitations, most notably their limited specific capacity, affordability concerns, along with safety issues[7–9]. On the other hand, Na-ion batteries (SIBs) are inhibited by insufficient capacity as well as by severe volume expansion and electrode breakdown[10,11]. For this purpose, it is widely recognized that the electrodes design-related components such as type of active materials and its thickness, the volume ratio of the active material, and the atom size are the major parameters affecting the electrochemical battery performance and its energy and power densities[12–15]. Therefore, designing and fully

analyzing alternative high-rate active materials for both LIBs and SIBs represents the most important issue to be tackled in this field.

Recently, numerous emerging two-dimensional (2D) nano-materials have been engineered and synthesized. Out of them, the borophene and boron nitride (BN) monolayers have been recognized as the most versatile 2D lightest materials so far. They consist of a non-oxidizing monolayers made by alternating bonds of equal amounts of B and N atoms[16–21]. In contrast to 2D borophene-based monolayers, notably puckered-triangular phase (β_{12} -borophene) and planar-striped phase (χ^3 -borophene), which are extensively investigated as high-efficiency battery electrodes within the Li-ion and Na-ion batteries,[19,22,23] 2D boron nitride monolayer has been poorly explored for the electrochemical energy conversion and storage since its initial prediction to its feasible synthesis. That is mostly attributed to the wide band-gap of around 4–6 eV and to the electronic nature of the boron nitride material [24,25]. Nevertheless, the distinctive feature of 2D boron nitride material consists in its tunable surface-chemistry and adjustable bandgap. Within last decade, the electronic band gap of boron nitride material has been demonstrated to be efficiently adjusted through different approaches, like a functionalization, chemical and physical modulation, by

* Corresponding author.

E-mail address: rajeev.ahuja@physics.uu.se (R. Ahuja).

<https://doi.org/10.1016/j.electacta.2022.140491>

Received 30 January 2022; Received in revised form 29 March 2022; Accepted 1 May 2022

Available online 3 May 2022

0013-4686/© 2022 The Author(s). Published by Elsevier Ltd. This is an open access article under the CC BY license (<http://creativecommons.org/licenses/by/4.0/>).

In light of the feasibility and practicality of 3D-based porous materials for electrochemical energy storage systems compared to their 2D-based monolayers counterparts, it becomes interesting to ask whether we can develop novel 3D porous BN networks selectively assembled from the h-BN monolayer to broaden their applicability as electrodes for high-performance Li/Na-ion batteries. A wide range of computational models for designing 3D micro-porous BN have been widely reported within the literature to identify innovative approaches to synthesize 3D porous BN materials featuring adjustable pore-sizes [29,30,32,33] and despite the tremendous progress in exploring and investigating selected 3D porous materials such as 3D porous carbon and boron based allotropes, 3D porous MXene materials for high performance battery electrodes, [34–38] BN based 3D porous networks have not been yet investigated for energy-storage applications. Motivated by the previous prediction of new 3D porous BN networks with possessing adjustable characteristics, that can be assembled from zigzag BN nanoribbons

2. Methods and computational details

The geometric structure, stability, and electronics along with the electrochemical characteristics of 3D porous boron nitride (3D lz1-BN) are explored through the density functional theory (DFT) as implemented in the Vienna Ab-initio Simulation (VASP) Package[40]. The generalized-gradient approximations were employed along with Perdew-Burke-Ernzerhof (GGA-PBE)[41]. The Projector-Augmented-Wave (PAW) method was applied to tackle the ions and electrons interactions[42]. The plane-wave basis set at a threshold kinetic-energy of 500 eV and the convergence criteria while optimizing the lattice-parameter and atomic-positions were fixed at 10^{-5} eV and 10^{-3} eV/Å for energy and force, respectively. The Brillouin-zone is taken by

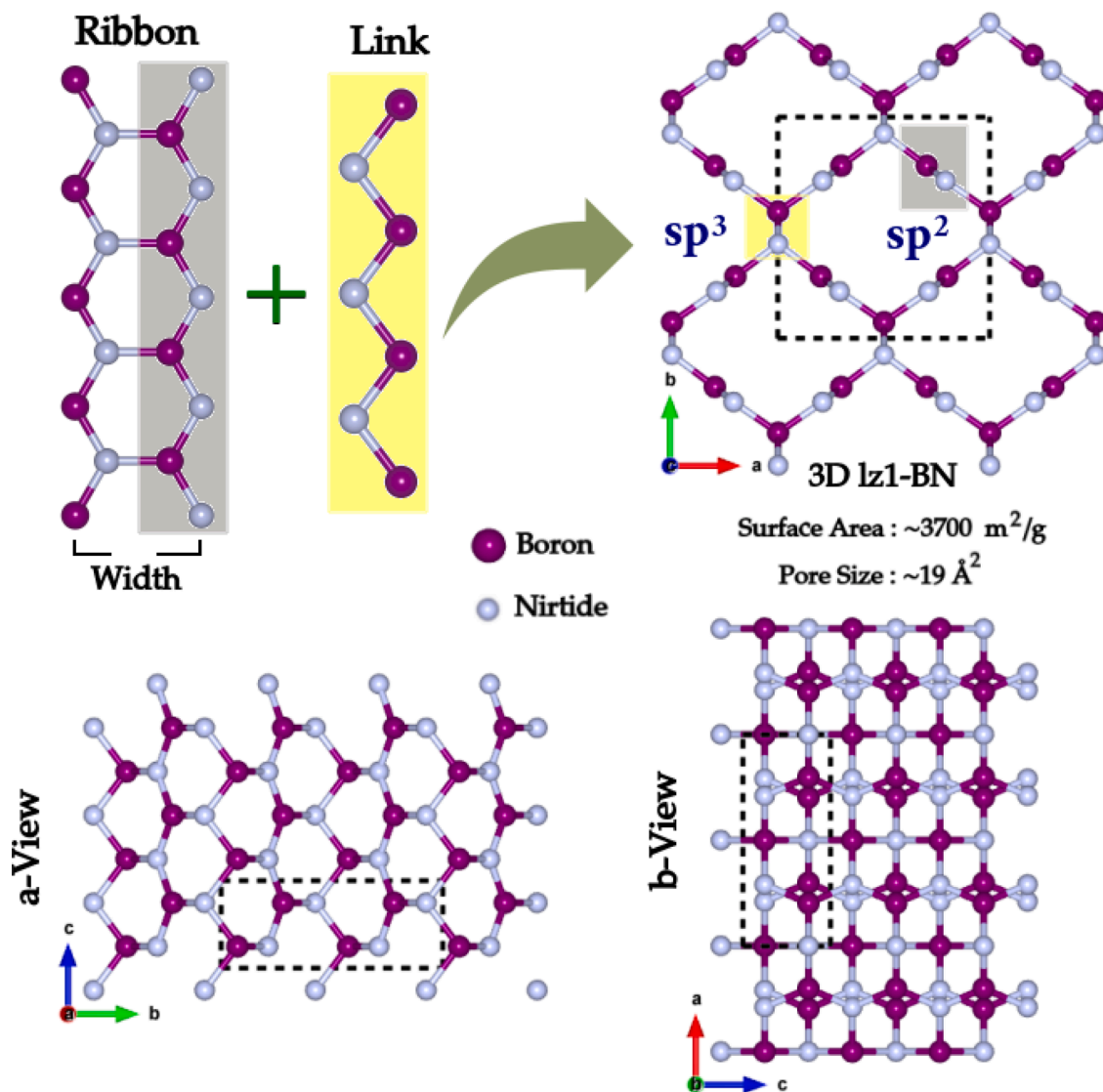


Fig. 1. Schematic illustration 3D porous BN lz1-BN material fused with zigzag BNNRs and sp^3 BN link chain. The Unit cell in different views (a, b and c) of 3D porous lz1-BN.

kpoints at 0.02 \AA^{-1} based on the Monkhorst-Pack scheme were assumed [43]. The electron-charge transfer is examined through the Bader charge algorithm [44]. In order to check the thermal stability of the 3D porous lz1-BN before/after the lithiation and sodiation at high-temperature, ab-initio molecular dynamics (AIMD) simulations in the NVT set with a time-scale of 10 ps at 500 K and 1000K were performed. Additionally, for the kinetic properties of Li(Na), climbing Image Nudged elastic band method [45]. For crystal orbital Hamiltonian population (COHP) analysis for chemical bonding information, we have used The Lobster software [46].

3. Results and discussion

3.1. Geometric structure and stability

The fully optimized crystal structure of 3D porous lz1-BN with three different views is displayed in Fig. 1. The unit cell of 3D lz1-BN is formed by zigzag BN nanoribbon (BNNR) and linked with BN chain as shown in Fig. 1. The adjacent zigzag BNNR is linked with the BN chain. It was also seen that the linked BN chain shows sp^3 hybridization whereas zigzag BNNR displayed sp^2 hybridization. The optimized lattice constant are found to be $a = 6.08$, $b = 6.36$ and $c = 2.51 \text{ \AA}$ which is good consistent with previous literature [39]. The optimized bond lengths between B-N are 1.57 \AA (along with linked BN chain), 1.43 \AA (along zigzag BNNR). As a result of its uniform porous interconnected network, 3D porous lz1-BN exhibits a low density of 2.547 g/cm^3 and volume of 16.932 \AA^3 in line with the findings obtained in previous work [39] and smaller compared to some other 3D porous networks as summarized in the Table 1.

Further to check the structural stability, we have investigated the ab initio molecular dynamics simulations using NVT ensemble for 10 ps at two different temperatures i.e. 500 K and 1000 K. The AIMD simulations are presented in Fig. 2. It was seen that initially shows higher energy fluctuations with respect to simulation time whereas, after 5 ps, the fluctuations in energy are relatively very less at both considered temperatures. It means that, at 10 ps simulation time, the structure of 3D porous lz1-BN is fully relaxed. The inserted structures in Fig. 2 displayed the snapshot at 500 K and 1000 K after 10 ps. From Fig. 2, there is no breaking of bonds between the B-N atoms. It means that the considered 3D porous lz1-BN structure is thermally stable. From previous literature, it was reported that the 3D porous lz1-BN structure shows energetically,

Table 1

Comparison of geometrical parameters including space group, lattice constants, Volume, total energy and density of 3D lz1-BN with selected 3D materials reported recently.^a

3D Structures	Space group	Lattice constants (\AA)	Volume (\AA^3)	Total-energy (eV/atom)	Density (g/cm^3)
lz1-BN	Amm2	6.079, 6.356, 2.510	16.932	-8.656	2.547
lz2-BN	Ima2/46	4.927, 3.169, 8.045	20.702	-8.567	2.624
Graphite	P6/mmm	2.462, 2.462, 7.324	8.471	-9.21	2.259
Diamond	Fd $\bar{3}$ m	4.346, 4.346, 4.346	5.518	-9.09	3.601
(P-6M2)-BN [29]	P-6M2	6.344, 6.344, 2.479	10.8	—	—
IMM2-BN [29]	IMM2	6.345, 2.480, 15.307	12.05	—	—
dz2-BN [39]	IMA2	4.934, 3.250, 8.037	15.28	—	—
dz4-BN [39]	AMA2	4.985, 3.393, 16.618	16.48	—	—

^a The "—" indicates that these data are unavailable.

mechanically and dynamically stable [39].

3.2. Mechanical properties

A further vital aspect to confirm the strength of the newly designed materials is the mechanical stability, that could be ascertained through the calculation of the elastic constants. From the strain energy approach, the derived elastic constants of 3D porous lz1-BN are consistent with the Born-Huang criteria [47]:

$$C_{11} > 0, C_{11}C_{22} > C_{12}^2 \quad (1)$$

$$C_{11}C_{22}C_{33} + 2C_{12}C_{13}C_{23} - C_{11}C_{23}^2 - C_{22}C_{13}^2 - C_{33}C_{12}^2 > 0 \quad (2)$$

$$C_{44} > 0, C_{55} > 0, C_{66} > 0 \quad (3)$$

Table 2 summarize the computed elastic constants for 3D lz1-BN, It can be seen that the elastic constant satisfy the above criteria, which confirms the mechanical strength. The symmetric stiffness matrix consists of:

$$C_{ij} = \begin{bmatrix} C_{11} & C_{12} & C_{13} & 0 & 0 & 0 \\ & C_{22} & C_{23} & 0 & 0 & 0 \\ & & C_{33} & 0 & 0 & 0 \\ & & & C_{44} & 0 & 0 \\ & & & & C_{55} & 0 \\ & & & & & C_{66} \end{bmatrix}$$

For the sake of comparison, the derived elastic constants for newly designed 3D β_{12} -borophene and 3D B $_7$ P $_2$ structures appear to be ultra-low, indicating the high mechanical stability of the 3D lz1-BN porous structure. The bulk-modulus (B), shear-modulus (G), and Young-modulus (Y) are examined based on the Voigt Reuss Hill method [48] and found to be 269.1, 179.1, and 439.8, respectively. By contrast, other 3D structures, including graphite maintained by weak van-der-Waals interactions along a pure sp^2 chemical bond, display an ultra-low shear modulus, indicating the high softness of this structure. Meanwhile, diamond from pure sp^3 bonding represents the hardest known solid material. Consequently, we believe that the 3D porous structure of lz1-BN with mixed sp^3 - sp^2 chemical bonds that we designed has the potential to provide intriguing mechanical properties. By definition, the crystal structure can be ductile ($B/G > 1.75$), or brittle if not [49]. The derived B/G ratio is 1.505, implying that the 3D porous lz1-BN structure is brittle.

Throughout the charge and discharge process, it is possible that the battery electrode materials will fracture, leading to failure of rechargeable battery. Therefore, we have examined the tensile strength so as to unveil the highest stress that the 3D porous lz1-BN can withstand. The Fig. 3 illustrate the snapshots of 3D porous lz1-BN structures at failure with corresponding tensile strengths as a function tensile strains along the x-, y-, and z-directions. Based on the crystal lattice of 3D lz1-BN, three different directions are taken to investigate the optimal tensile strength. The strength is examined for various degrees of tensile-strain (0-60%) according to the stress-strain approach. The computed tensile-strengths along the x-, y- and z-directions are 60.64 GPa for a 45% strain, 66.34 GPa for a 47.5% strain, and 82.64 GPa for a 25% strain, respectively. The above findings indicate an anisotropy in the tensile strengths of 3D lz1-BN. The weakest tensile strength resides in the x-direction, suggesting that the 3D lz1-BN structure breaks along the x-direction immediately when the tensile-strength exceeds 60.64 GPa. These computed values are more better than some 3D BN polymorph [31]. Consequently, the crystal structure of 3D porous lz1-BN can retain its structural stability along a large values of tensile-strains during charge/discharge process.

3.3. Chemical bonding analysis

In addition, we have used crystal orbital Hamilton population

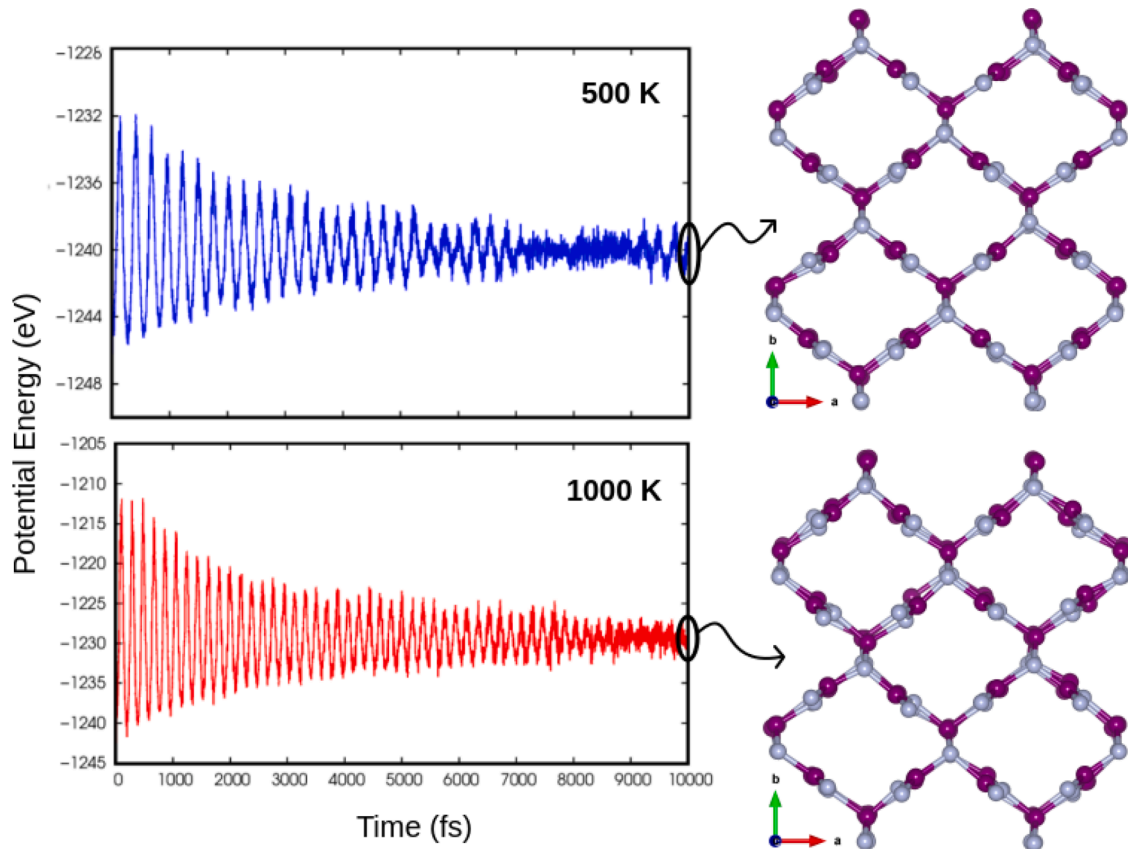


Fig. 2. The fluctuation of potential energy at 500 and 1000 K using Ab Initio Molecular dynamic simulation for 3D porous lz1-BN system and the resulting structures at the end of the simulation.

Table 2

Computed independent elastic constants C_{ij} (in GPa) of 3D porous lz1-BN material.

	C_{11}	C_{22}	C_{33}	C_{44}	C_{55}	C_{66}	C_{12}	C_{13}	C_{23}
lz1-BN	431.7	306.1	966.8	235.1	194.6	215.5	248.6	108.7	76.4
β_{12} -borophene [38]	135.7	137.0	396.4	57.6	60.3	59.2	62.5	21.5	21.8
B_7P_2 [38]	69.7	180.8	70.1	39.3	43.7	8.5	18.0	43.5	18.1

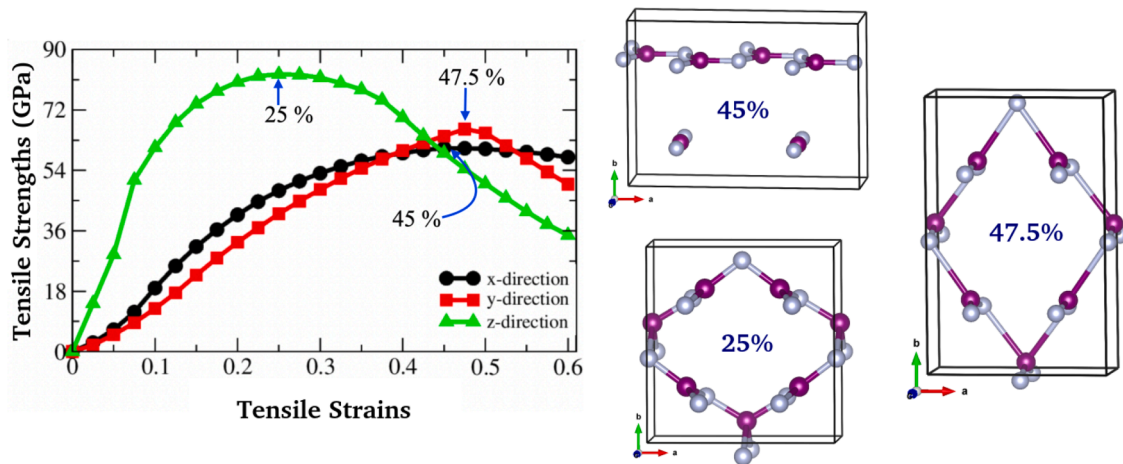


Fig. 3. Mechanical properties of 3D porous lz1-BN, calculated tensile-strengths Vs tensile-strains along the (x/y/z)-directions with corresponding snapshot of 3D lz1-BN structures at failure stress.

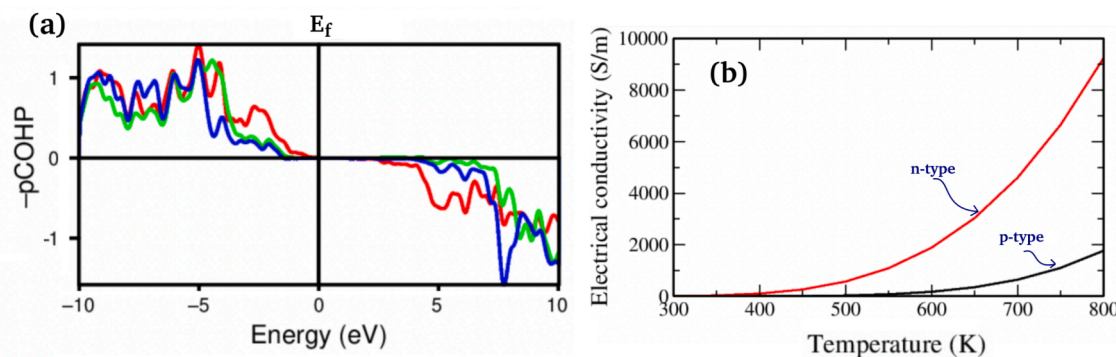


Fig. 4. (a) Projected crystal orbital Hamilton population (-pCOHP) analysis for 3D lz1-BN material of the B-N pair. The zero vertical line shows the Fermi energy. The -pCOHP gives information about the contribution of a particular bond (bonding or anti-bonding) to the band energy. Plot show bonding contribution in the up side (+y-axis) and the anti-bonding contribution is down side (-y-axis). The color red-1.43 Å, green-1.57 Å and blue-1.53 Å represents the bond pair between B and N atom. (b) Temperature dependent electrical conductivity for n-type (red line) and p-type (black line) carriers. (For interpretation of the references to colour in this figure legend, the reader is referred to the web version of this article.)

(COHP) analysis to determine the chemical binding information between atom pairs. The COHP analysis provides information about bonding, anti-bonding and non-bonding contributions into the different orbital pair interactions to the band structure. Fig. 4 shows the projected COHP profile which gives the quantitative estimation of the strength of bonds in the structure. The positive values on the y-axis represent the bonding nature whereas the negative y-axis shows the anti-bonding nature (see Fig. 4). Based on the 3D lz1-BN structure as shown in Fig. 1, B-N atom pairs have different bond lengths therefore, we have calculated the COHP profile for each atom pair. It can be clearly seen that there are no anti-bonding contributions present below the Fermi level in the B-N pairs but only the anti-bonding contribution is present above the Fermi level. Such type of characteristics is present in the strong covalent bonding interactions between the B-N atom pairs. Also, we have calculated the interacted COHP values which are found to be -11.24, -8.82 and -8.84 eV for atom pair bond lengths of 1.43, 1.53, and 1.55 Å, respectively. The negative values of -ICOHP values displayed the strong covalent bonding interactions in the B-N pair. Such types of strong covalent interaction show higher stability and exhibit better catalytic performance [50].

3.4. Electrical conductivity and electronic properties

The electrical conductivity of battery electrodes has a significant effect as a key driver of their electrochemical performance and operating capacity. In addition, the energy band gap, which is taken as a relevant factor in the electronic properties analysis, strongly affects the conductivity of the material. A correlation between the two factors can be derived according to the formula below:

$$\sigma \propto \exp\left(-\frac{E_g}{2K_B T}\right) \quad (4)$$

Where, σ , T , E_g refers to the electrical conductivity, the temperature, and energy bandgap, K_B denote the Boltzmann's constant. One can perceive that the electronic band gap and conductivity are inversely related to each other, i.e. the smaller the band gap, the higher the electrical conductivity and, conversely. In this background, the wide band gap of about 4.36 eV reported in 2D h-BN monolayer leads to a lower electrical conductivity, which hinders its applicability as a battery electrode. In the case of a 3D porous lz1-BN material, a smaller electronic band gap than that of 2D h-BN will yield a higher electrical conductivity. Furthermore, we have calculated the electrical conductivity of pristine 3D porous lz1-BN structure based on Boltzmann transport formalism [51]. The Fig. 4(b) depict the temperature dependent electrical conductivity for n-type and p-type 3D porous lz1-BN. It is obtained that the electrical conductivity at 300 of p-type carriers equal

to 0.0399399 S/m whereas n-type carriers is about 7.102226 S/m and linearly enhances with increasing the temperature.

To understand the electronic properties of 3D porous lz1-BN material, we have investigated the orbital contributed electronic band structure as well as projected density of states (PDOS) and electron localization function. Fig. 5a shows the ELF of 3D lz1-BN material which represents the bonding nature between the atoms. It was clearly seen that the cloud of electron density is localized between the bond of B and N atoms. It means that B and N form strong covalent bonding. Such types of materials provide an excellent mechanical property. Also, the calculated electronic band structure and PDOS are presented in Fig. 5b. From the electronic band structure, 3D lz1-BN material shows a direct band gap of 0.80 eV at high symmetry point Z. The top of the valence band maximum is made by N p-states whereas the bottom of the conduction band minimum is formed by B p-states. It means that N p-states and B p-states are mainly responsible to form a direct bandgap in 3D lz1-BN material. From PDOS, we found that the N p-states is mainly dominated near the Fermi level in the valence band whereas the main contribution comes from B p-states in the bottom of the conduction band as same as appears in the projected band structure.

3.5. Adsorption energy of lithium/sodium on 3D lz1-BN electrode

As previously mentioned, 2D graphene-like boron nitride (BN) is among the most extensively explored and implemented 2D materials family for its broad applicability in a variety of devices. Yet, its eventual relevance as battery electrode for electrochemical energy storage systems is constrained by its large band gap which limit its electrochemical performances. Hence, we are going to investigate for the first time, an alternative stable allotrope of boron nitride 3D porous lz1-BN which is made by assembling the zigzag BN nanoribbons (BNNRs), [39] which is predicted recently and confirmed to be stable chemically, dynamically and thermally, unveiling its unique electrochemical efficiency as a battery electrode for Li/Na-ion batteries.

Additionally, considering that both Boron and Nitride belong to very light elements with a small molecular weight of about 10.811 and 14.0067 a.u, respectively, as well as the uniformly distributed pores in the 3D porous lz1-BN structure hints at their great suitability as battery electrode and could potentially reach an exceptional electrochemical performance for lithium and sodium-ion batteries. Accordingly, We shall first investigate the adsorption strength of a single Li^+ and Na^+ on suitable adsorption sites of the 3D porous lz1-BN structure according to the equation given below:

$$E_{ads} = E_{(Li,Na)@3D-lz1-BN} - E_{3D-lz1-BN} - \mu_{(Li,Na)} \quad (5)$$

Where $E_{(Li,Na)@3D-lz1-BN}$ and $E_{3D-lz1-BN}$ refers to the total energies of the

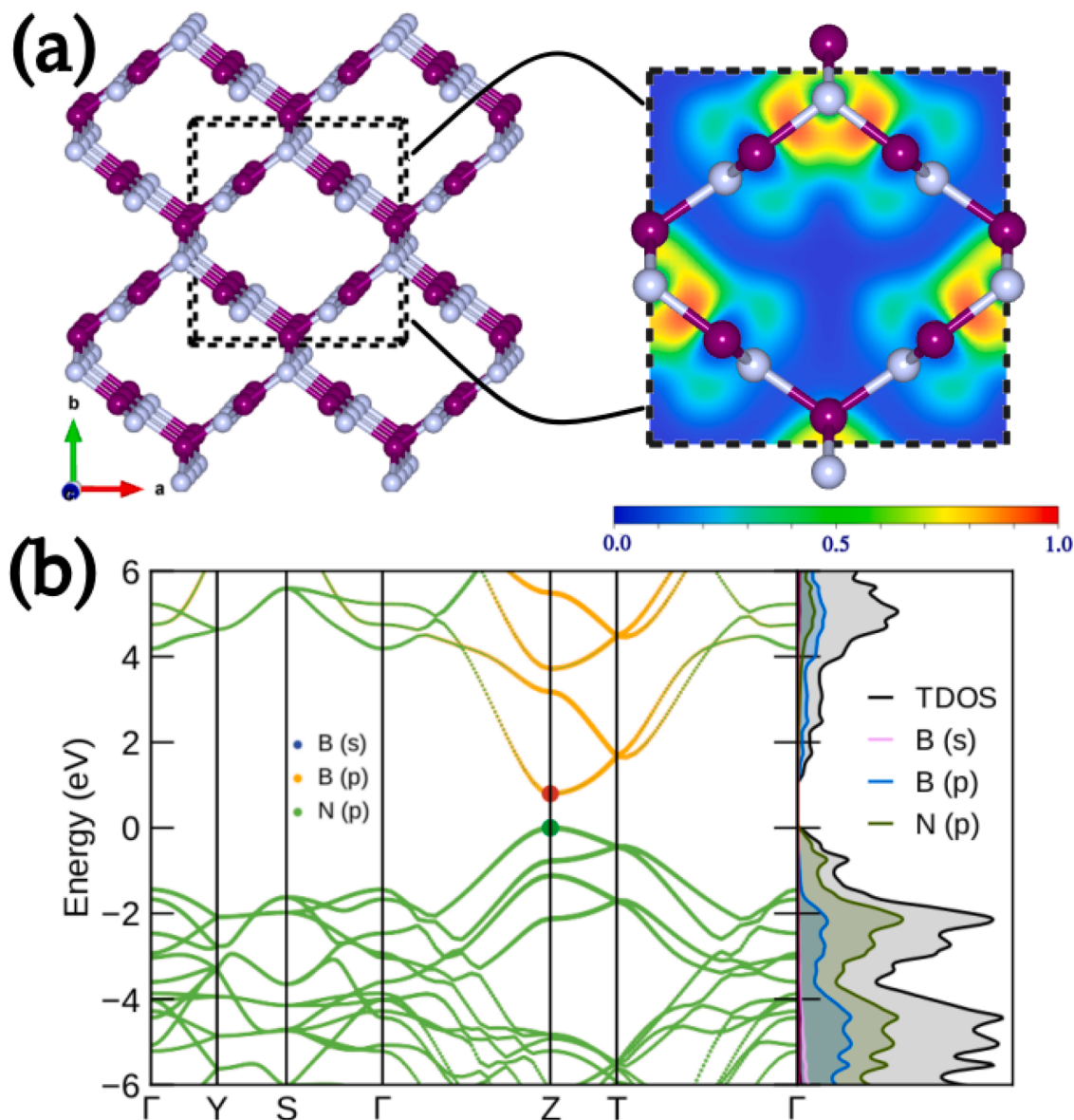


Fig. 5. (a) Schematic illustration of electron localization function (ELF) and (b) projected band structure with corresponding projected density of states for 3D lz1-BN material.

3D porous lz1-BN structure with and without the adsorption of Li^+ and Na^+ , respectively, $\mu_{(\text{Li,Na})}$ represents the chemical potential of (Li, Na)-atom. Taking advantage of the crystalline symmetry, five adsorption sites for both Li- and Na-ions were initially identified in this study, which included two hollow-sites (S1 and S2), one top-site (S3) of B-atom, and one top-site (S4) on N-atom in B_4N_4 -ring, and one bridge-site (S5) located between boron and nitrogen atoms, as illustrated in Fig. 6. Within these screened active sites, it is noticed that all the computed adsorption strengths are negative which indicates the scattering distribution of the adsorbed Li/Na-atoms in the 3D porous lz1-BN structure instead of their clustering. All the computed adsorption strengths are summarized in Table 3 with corresponding charge transfer of Li and Na to the material. One can obviously notice that the S1 site shows the lowest adsorption strength of -2.323 and -0.778 eV for Li- and Na-atom, respectively. For comparison purposes, these values are significantly higher compared to the previously reported 3D porous materials, such as 3D porous Si_2BN (-0.85/-0.84 eV for Li/Na) [52], 3D porous Tetragonal C_{24} (-1.09 eV for Na) [53], 3D- β_{12} -borophene (-1.14/-1.31 eV for Li/Na) [38], and 3D- B_7P_2 (-1.19/-0.95 eV for Li/Na) [38].

Further advancement of high-efficiency Li and Na-ion batteries

fundamentally relies on the capability of their anode, and more specifically on the charging and discharging operation, which is typically determined by the Kinetic properties of electron transfer. Accordingly, the charge density difference of single Li and Na on the lowest adsorption site of the 3D Porous lz1-BN structure has been investigated by means of the given formula:

$$\Delta\rho = \rho_{(\text{Li,Na})@3\text{D-lz1-BN}} - \rho_{3\text{D-lz1-BN}} - \rho_{\text{Li,Na}} \quad (6)$$

Where, $\rho_{(\text{Li,Na})@3\text{D-lz1-BN}}$ and $\rho_{3\text{D-lz1-BN}}$ are the charge densities of the 3D porous lz1-BN system after and before the adsorption of single Li and Na atom, $\rho_{\text{Li,Na}}$ is the charge density of Li and Na atom within the same system with no further shape-relaxation. The Yellow and cerulean zones are depicted in Figure. 7(a,b) refers to the charge accumulation and depletion for Li and Na-ions, respectively. The charge accumulation zone is situated near the Li and Na atom and on the surface of the 3D porous lz1-BN structure, while the depletion zone slightly surrounds the Li- and Na-atom and on sp^3 linked zigzag BNNRs, thereby showing that the charge gain by the 3D porous lz1-BN material and the charge loss by the Li- and Na-atom; this resulted in increased electronegativity of both

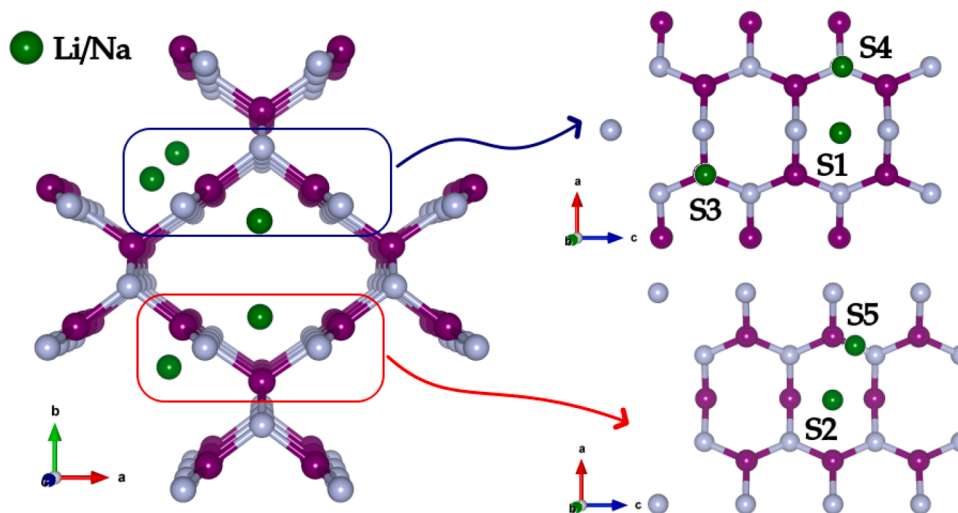


Fig. 6. Potential Electrochemical active sites for the adsorption of Li and Na on the $1 \times 1 \times 3$ supercell of 3D lz1-BN.

Table 3

Active sites and binding strength of single Li/Na-atom adsorbed on 3D lz1-BN material, ratio of binding energy to cohesive energy of Li/Na, binding height and charge transfer Q ($|e|$) of Lithium/Sodium adsorbed on different binding sites.

Systems	Active Site	E_b (eV)	Q_{Li} (e)	Q_{Na} (e)
3D lz1-BN@Li	S1	-2.323	0.913	–
	S2	-2.217	0.896	–
	S3	-2.252	0.907	–
	S4	-2.125	0.891	–
	S5	-1.914	0.884	–
3D lz1-BN@Na	S1	-0.778	–	0.885
	S2	-0.715	–	0.879
	S3	-0.726	–	0.880
	S4	-0.579	–	0.876
	S5	-0.502	–	0.877

B- and N-atoms relative to that of the Li- and Na-atoms. Further, the electron charge transfer is carried out via Bader charge analysis with the outcomes summarized in the Table 3. It found that Li- and Na-atom adsorbed at the most suitable active site loses a mean electron-charge of 0.913 and 0.885 $|e|$, respectively, thereby affirming the cationic character of the Li- and Na-ions.

On the other hand, a more in-depth elucidation of the binding and electronic behavior upon Li- and Na-atom adsorption were investigated via the projected band-structure along with the respective partial density of state, which can be seen in Fig. 7(c,d). From our analysis, it is obvious that the host material shifted from the semiconductor nature to metallic upon a single Li- and Na- adsorption occurring with a clear contribution coming from the Li- and Na-atom around the Fermi-level. This leads to a significantly improved electrical conductivity with a quick electron transfer within the negative electrode during the charge-discharge process, which fulfills a pivotal role in the high-rate capability in Li-ion and Na-ion batteries.

3.6. Li/Na storage capacity and theoretical voltage profile

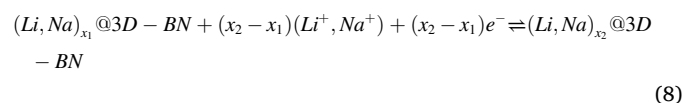
With the aim of more deeply probing the electrochemical capabilities of 3D porous lz1-BN host material for Li/Na-ion batteries, the Li/Na-storage capacity and theoretical voltage profile were surveyed by gradually inserting Li/Na-ions on the host material structure. A sequence of intermediate concentrations of $(Li/Na)_x@BN$ (with $x = 0.055, 0.111, 0.167, 0.222, 0.278, 0.333, 0.389, 0.444, \text{ and } 0.500$) are taken into account. The average adsorption strength E_{ads}^{Avg} of $x(Li/Na)$

ions inserted on host material were calculated by the given equation:

$$E_{ads}^{Avg} = \left(E_{(Li/Na)_x@3D-BN} - E_{3D-BN} - x\mu_{(Li/Na)} \right) / x \quad (7)$$

From the Fig. 8(a,b) (red-line), one can clearly notice that the average adsorption strength of $(Li, Na)_x@3D-BN$ decreases gradually with respect to the $x(Li, Na)$ -concentration and that the E_{ads}^{Avg} obtained in case of Li-atoms are higher than those obtained in case of Na-atoms, that is mainly due to the reduced electrostatic interactions between the (Li, Na) and the host material along with the strengthened repulsion of the (Li, Na)-atoms in higher-concentrations. Additionally, the binding energies from all concentrations over the full charging process are consistently negative, thereby inhibiting the creation of (Li, Na)-dendrites.

Another pivotal point to assess the high-performance of the rechargeable battery is the voltage profile. Conventionally, the lithiation/de-lithiation and sodiation/de-sodiation process of the active electrode can be regarded as the following half cell reaction:



The average voltage profile for 3D porous lz1-BN at each equilibrium stage of the reaction (8) can be defined by the given formula: [62,63]

$$V(x) \approx - \frac{E_{(Li/Na)_x@3D-BN} - E_{3D-BN} - x\mu_{(Li/Na)}}{Z.x.e} \quad (9)$$

The computed average theoretical voltage profile as a function of x (Li, Na)-ions in the 3D porous lz1-BN were depicted with a blue-line in the Fig. 8(a,b). one can obviously notice initially that the $V(x)$ for all the intermediate concentrations are positive, supporting the suitability of the 3D porous lz1-BN as anode material for (Li, Na)-ion batteries. The theoretical voltage profile shows a decreasing curve going through eight insertion plateaus with an average voltage of 1.053 Vs Li^+/Li and 0.331 Vs Na^+/Na , that lies within the range of the required potential voltage in order to achieve a high power density upon the charge and discharge process [64].

The highest theoretical capacity (C_{th}) for (Li^+, Na^+) -ions insertion in 3D porous lz1-BN can be derived following the equation given as:

$$C_{th} = \frac{x_{max} \cdot z \cdot F}{M_{3D-BN}} \cdot 10^3 \quad (10)$$

Where x_{max} denote the highest number of (Li^+, Na^+) -ions inserted in 3D porous lz1-BN, $M_{B_2N_2}$ refers to the molar-mass of the pristine system.

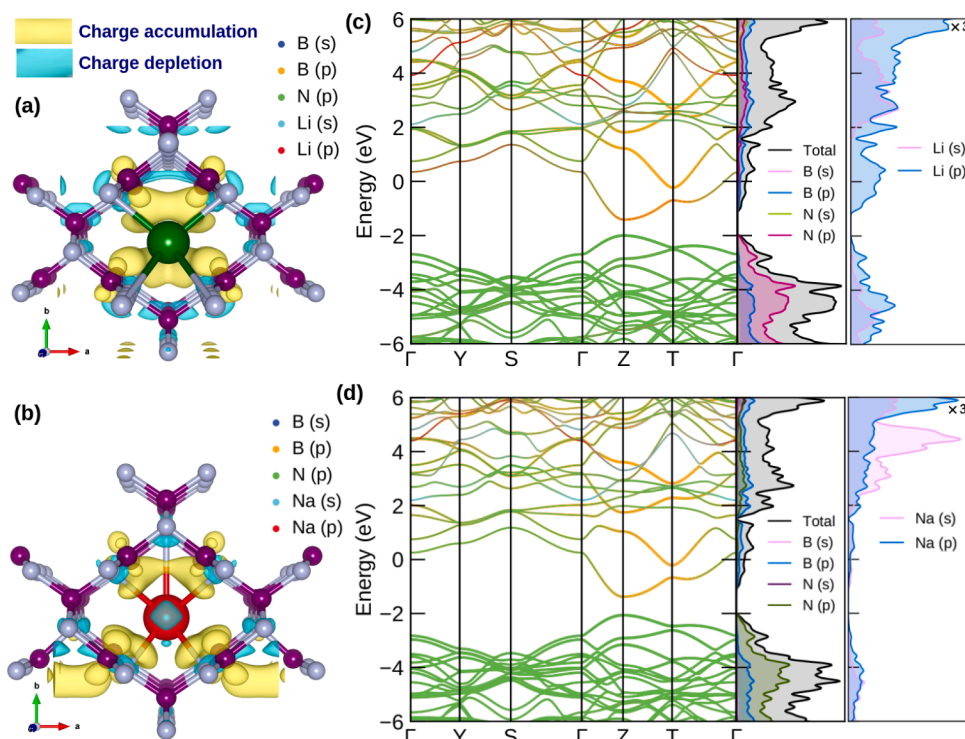


Fig. 7. 3D isosurface distributed charge density plot for (a) Li- and (b) Na- atom adsorbed at the most stable binding site (S1) on 3D porous lz1-BN. The Yellow and cerulean refer to the electron accumulation and depletion, respectively, and the charge transfer from the Li- and Na-atom to 3D lz1-BN are about 0.913 and 0.885 $|e|$. (c,d) The Projected band structure with a corresponding total and partial density of state for 1Li@lz1-BN and 1Na@lz1-BN systems, respectively.

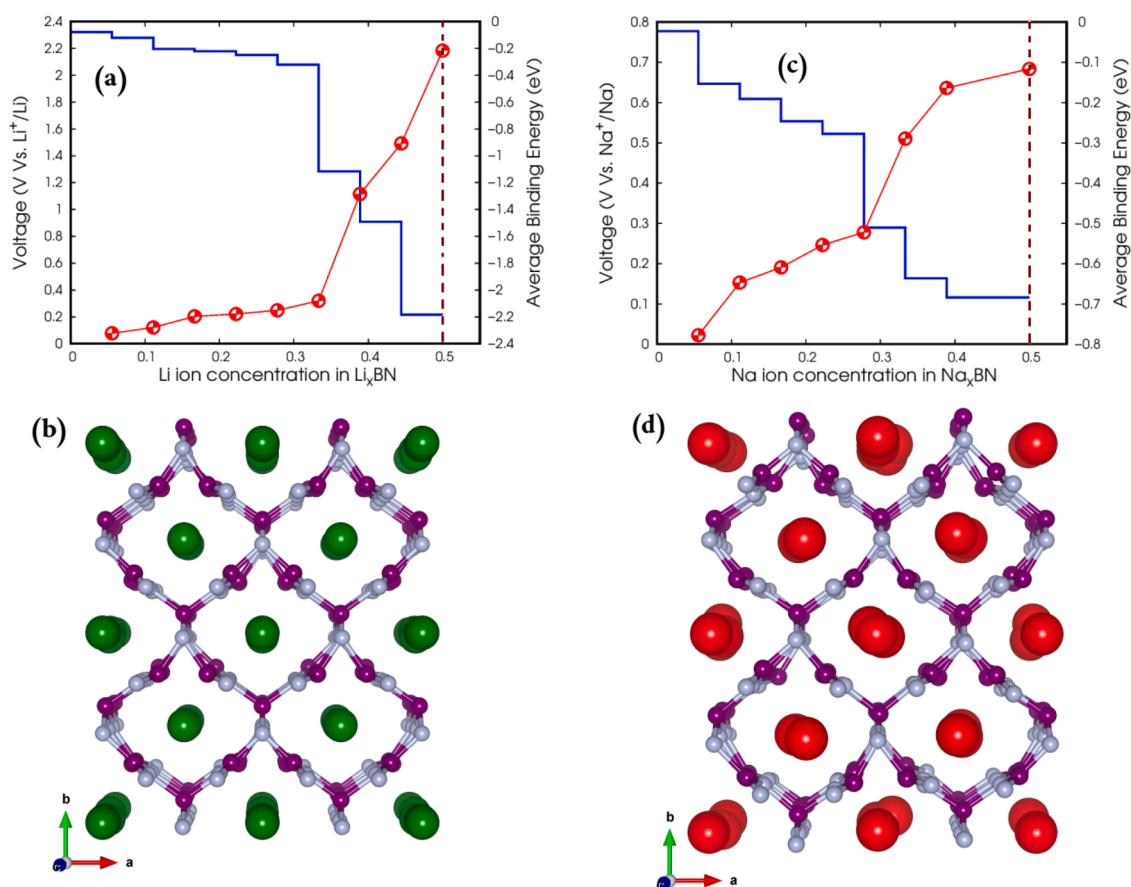


Fig. 8. Average adsorption strengths and Open-circuit voltages and corresponding Highest Li/Na-concentration configuration of (a,b) Li-ions and (c,d) Na-ions adsorbed on 3D lz1-BN as functions of the Li/Na-ion concentration x .

Table 4

Electrochemical performance comparisons of 3D lz1-BN anode material with recently reported 3D anode materials: Theoretical storage Capacity (in mAh/g), Diffusion Barrier (in eV), Average Open-Circuit Voltage (in V), Volume Change (in %), and electronic band behavior after Li/Na adsorption.^b

3D Anode materials	Battery type	Storage capacity	Diffusion barrier	Average OCV	Volume change
lz1-BN	Li	539.94	0.416	1.053	0.761
	Na	539.94	0.270	0.331	2.231
graphite [54,55]	Li	372	0.40	0.11	10
	Na	<35	0.30	—	—
Janus-graphite [56]	Li	—	—	—	—
	Na	≈332	<0.2	0.05	0.5
N-hole graphite [57]	Li	—	—	—	—
	Na	482	0.59	0.26	~3.0
bco-C ₁₆ [58]	Li	558	0.53	0.23	13.4
	Na	—	—	—	—
m-C ₁₆ [59]	Li	588	0.25	0.56	3.6
	Na	—	—	—	—
3D-BPC ₂ [60]	Li	407	0.29	0.48	0.25
	Na	406	0.05	0.50	1.15
3D Si ₂ BN [52]	Li	512	0.44	0.27	2.5
	Na	341	0.19	0.15	2.7
t-C ₂₄ [53]	Li	232.65	0.13	0.54	—
	Na	—	—	—	—
SiC ₄ -I [61]	Li	—	—	—	—
	Na	176.3	0.410	0.55	0.57

^b The "—" indicates that these data are unavailable.

As a result, the highest evaluated theoretical capacity derived from Li and Na insertion in 3D porous lz1-BN anode material is approximately 539.94 mAh.g⁻¹, which is higher compared to some typical 2D anode materials reported recently for Li- and Na-ion batteries as summarized in Table 4.

Upon the charge and discharge process, the battery electrode can undergo substantial volume growth along with eventual sputtering, leading to a fast decline in their capacity and a reduction in their life-time. Within this background, AIMD simulations were carried out to check the thermal stability of 3D porous lz1-BN anode upon the fully lithiated/sodiated process at high-temperature of about 800K with a total time-scale of 5ps as depicted in Fig. 9(a,b). One can noticed clearly from the resulting screen-shots at the end of the AIMD simulation that both systems maintain the original arrangement with small structural deformation and a small fluctuation in the potential energy. It can be also seen from the Fig. 9(a) that the original pores are obviously increased with no-distortion of B-N bond. Afterward, we have taken the both resulting structures from AIMD simulations and removed all the Li and Na-atoms in order to more understand the battery anode recovery process. A further AIMD simulations and an energy optimization calculation were performed, which gave the starting structure of 3D porous lz1-BN and thus confirms the reversible behavior of the 3D

porous lz1-BN as battery anode. The lattice constants, bond-lengths, and angles are in lines with the initial 3D lz1-BN crystal structure. Such a high stability and reversibility can be attributed to the *sp*³-chains which gives a strong mechanic properties and indicate the high stability of the fully considered lithiated and sodiated states at high temperature.

4. Activation barriers for Li⁺/Na⁺ electrode surface diffusion

Apart from the electro-conductivity, the Li/Na-ion scattering in the battery electrode constitutes other critical components that affect the battery operation [65]. As such, the dilute Li- and Na ion diffusion paths along with their respective minimum energy barrier were evaluated by climbing image NEB method. Based on the symmetry of the 3D porous lz1-BN structure, the activation barriers of Li⁺/Na⁺ along one typical path which consists of a Li⁺/Na⁺-migration along the c-direction as schematically illustrated in Fig. 10(a,b,c). The computed minimum Activation barriers for Li⁺ and Na⁺ are 0.416, 0.270 eV, respectively, which are in line with the values of adsorption strengths listed in Table 3. As a point of comparison, the derived minimum energy barriers for Li⁺ and Na⁺ on 3D porous lz1-BN material were found to be quite comparable to some recently reported 3D porous systems as given in Table 4.

5. Concluding remarks

We have systematically investigated the performance of 3D porous lz1-BN as an anode material for Li/Na-ion batteries. The 3D porous lz1-BN material shows high chemical and thermal stability compared to its 2D counterpart which based on the *sp*³-bonded B-N chains. Its found that the mixed *sp*²+*sp*³ hybridization in 3D porous lz1-BN material are the key processes that govern the BN materials' stability and physical/chemical characteristics. Using first-principles calculations along with ab-initio molecular dynamics simulations, we have calculated the adsorption energy, electronic band structures and density of states, Bader charge analysis, average potential, diffusion barrier of 3D lz1-BN material and its thermal stability during the lithiation/sodiation. It is found that the insertion of Li and Na into the 3D porous lz1-BN have good binding strength therefore it can be a superior anode electrode. Our calculations suggest that the interaction of Li and Na adatoms with 3D porous lz1-BN material shows a high electrical conductivity, good structural stability, high theoretical storage capacity as well as low charging voltage. The calculated barrier energies are 0.416, 0.270 eV with the diffusion of Li and Na adatoms into the 3D lz1-BN material, respectively. The open-circuit potential is found to be 1.053 V vs Li/Li⁺ and 0.331 V vs Na/Na⁺ with the insertions of Li and Na. The intercalation of Li and Na adatoms into the 3D porous lz1-BN materials leads to a high theoretical capacity of 539.94 mAh.g⁻¹ which is higher as

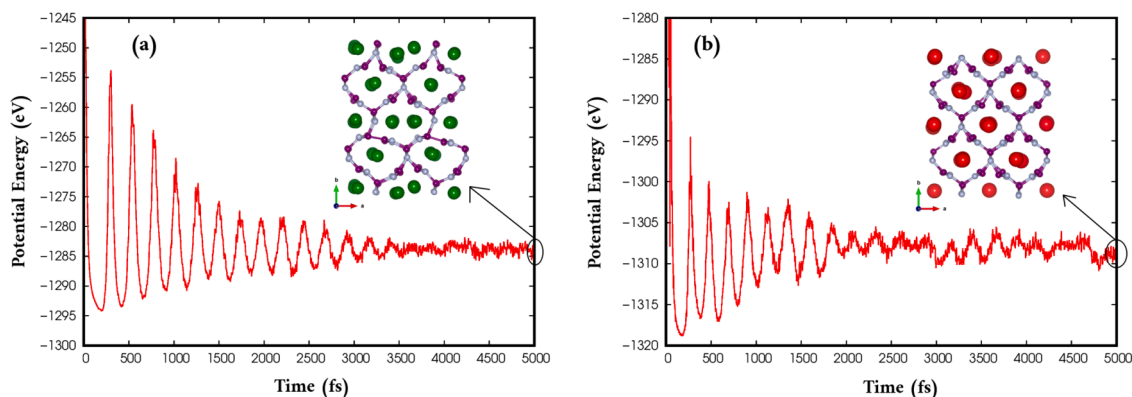


Fig. 9. (a,b) Variations in the potential energy for the highest lithiation and sodiation states of 3D porous lz1-BN upon the Ab-Initio Molecular Dynamic simulations at 800 K.

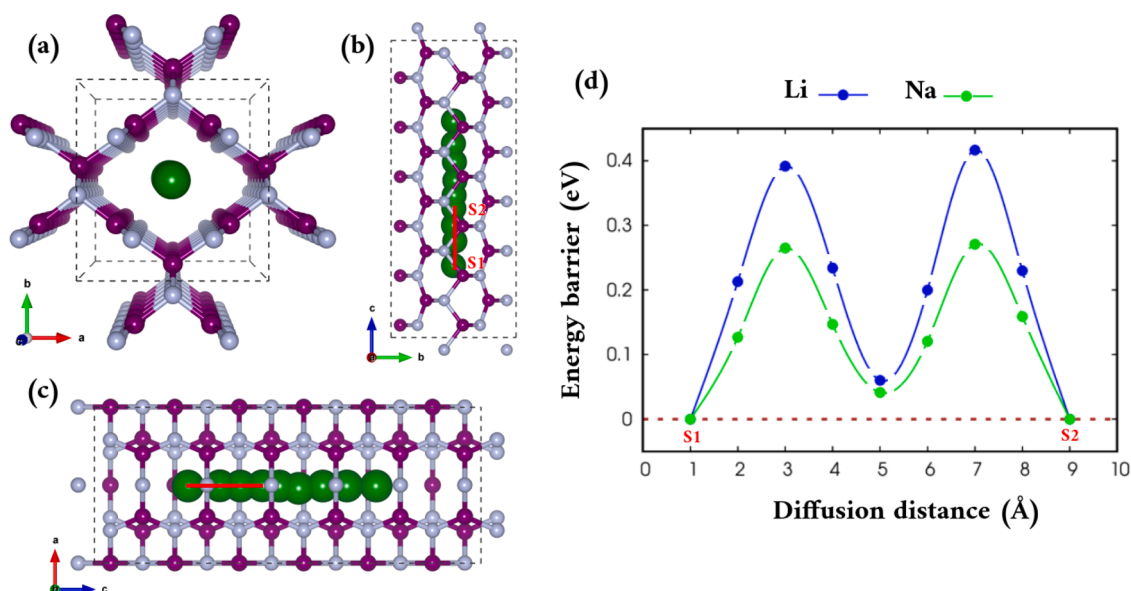


Fig. 10. (a,b,c) The schematic illustration of the considered Li/Na-ion migration pathway and (d) The corresponding diffusion energy barrier profile of Li/Na diffusion in 3D lz1-BN.

compared to some typical 2D anode materials. We hope that the findings investigations will shed light on the development of the new generation of Li and Na ion batteries for future technologies including electric vehicles, communication applications, and wearable electronics.

CRediT authorship contribution statement

Nabil Khossossi: Conceptualization, Data curation, Formal analysis, Investigation, Methodology, Validation, Visualization, Writing – original draft, Writing – review & editing. **Deobrat Singh:** Conceptualization, Data curation, Formal analysis, Investigation, Visualization, Validation, Writing – review & editing. **Wei Luo:** Conceptualization, Formal analysis, Validation, Visualization, Writing – review & editing. **Rajeev Ahuja:** Conceptualization, Formal analysis, Funding acquisition, Project administration, Resources, Software, Supervision, Validation, Writing – review & editing.

Declaration of Competing Interest

The authors declare that they have no known competing financial interests or personal relationships that could have appeared to influence the work reported in this paper.

Acknowledgments

We gratefully acknowledge computational resources from the Swedish National Infrastructure for Computing SNIC (2021/1-42) and HPC2N. N.K., D.S., W.L. and R.A. acknowledge the Swedish Research Council (VR-2016-06014 & VR-2020-04410) and J. Gust. Richert stiftelse, Sweden (2021-00665) for financial support.

References

- [1] M. Armand, J.-M. Tarascon, Building better batteries, *Nature* 451 (7179) (2008) 652–657.
- [2] Y. Bahari, B. Mortazavi, A. Rajabpour, X. Zhuang, T. Rabczuk, Application of two-dimensional materials as anodes for rechargeable metal-ion batteries: a comprehensive perspective from density functional theory simulations, *Energy Storage Mater.* (2020).
- [3] B. Dunn, H. Kamath, J.-M. Tarascon, Electrical energy storage for the grid: a battery of choices, *Science* 334 (6058) (2011) 928–935.
- [4] N. Khossossi, D. Singh, A. Ainane, R. Ahuja, Recent progress of defect chemistry on 2d materials for advanced battery anodes, *Chem. Asian J.* 15 (21) (2020) 3390–3404.
- [5] D. Singh, V. Shukla, N. Khossossi, A. Ainane, R. Ahuja, Harnessing the unique properties of mxenes for advanced rechargeable batteries, *J. Phys.* 3 (1) (2020) 012005.
- [6] P. Simon, Y. Gogotsi, Materials for electrochemical capacitors, *Nanosci. Technol.* (2010) 320–329.
- [7] Y. Chen, Y. Kang, Y. Zhao, L. Wang, J. Liu, Y. Li, Z. Liang, X. He, X. Li, N. Tavajohi, et al., A review of lithium-ion battery safety concerns: the issues, strategies, and testing standards, *J. Energy Chem.* 59 (2021) 83–99.
- [8] Z. Du, D.L. Wood, C. Daniel, S. Kalnaus, J. Li, Understanding limiting factors in thick electrode performance as applied to high energy density li-ion batteries, *J. Appl. Electrochem.* 47 (3) (2017) 405–415.
- [9] W. Huang, X. Feng, X. Han, W. Zhang, F. Jiang, Questions and answers relating to lithium-ion battery safety issues, *Cell Rep. Phys. Sci.* 2 (1) (2021) 100285.
- [10] J.-Y. Hwang, S.-T. Myung, Y.-K. Sun, Sodium-ion batteries: present and future, *Chem Soc Rev* 46 (12) (2017) 3529–3614.
- [11] R. Rajagopalan, Y. Tang, C. Jia, X. Ji, H. Wang, Understanding the sodium storage mechanisms of organic electrodes in sodium ion batteries: issues and solutions, *Energy Environ. Sci.* 13 (6) (2020) 1568–1592.
- [12] W. Mei, H. Chen, J. Sun, Q. Wang, The effect of electrode design parameters on battery performance and optimization of electrode thickness based on the electrochemical–thermal coupling model, *Sustain. Energy Fuel.* 3 (1) (2019) 148–165.
- [13] Y. Zhao, C. Ding, Y. Hao, X. Zhai, C. Wang, Y. Li, J. Li, H. Jin, Neat design for the structure of electrode to optimize the lithium-ion battery performance, *ACS Appl. Mater. Interface.* 10 (32) (2018) 27106–27115.
- [14] J. Joos, A. Buchele, A. Schmidt, A. Weber, E. Ivers-Tiffée, Virtual electrode design for lithium-ion battery cathodes, *Energy Technol.* (2021) 2000891.
- [15] M. Huang, M. Li, C. Niu, Q. Li, L. Mai, Recent advances in rational electrode designs for high-performance alkaline rechargeable batteries, *Adv. Funct. Mater.* 29 (11) (2019) 1807847.
- [16] Y. Lin, J.W. Connell, Advances in 2d boron nitride nanostructures: nanosheets, nanoribbons, nanomeshes, and hybrids with graphene, *Nanoscale* 4 (22) (2012) 6908–6939.
- [17] L.H. Li, Y. Chen, Atomically thin boron nitride: unique properties and applications, *Adv. Funct. Mater.* 26 (16) (2016) 2594–2608.
- [18] X.-F. Jiang, Q. Weng, X.-B. Wang, X. Li, J. Zhang, D. Golberg, Y. Bando, Recent progress on fabrications and applications of boron nitride nanomaterials: a review, *J. Mater. Sci. Technol.* 31 (6) (2015) 589–598.
- [19] Z.-Q. Wang, T.-Y. Lü, H.-Q. Wang, Y.P. Feng, J.-C. Zheng, Review of borophene and its potential applications, *Front. Phys.* 14 (3) (2019) 1–20.
- [20] A.J. Mannix, Z. Zhang, N.P. Guisinger, B.I. Yakobson, M.C. Hersam, Borophene as a prototype for synthetic 2d materials development, *Nat. Nanotechnol.* 13 (6) (2018) 444–450.
- [21] N. Khossossi, W. Luo, Z. Haman, D. Singh, I. Essaoudi, A. Ainane, R. Ahuja, Revealing the superlative electrochemical properties of o-b2n2 monolayer in lithium/sodium-ion batteries, *Nano Energy* (2022) 107066.
- [22] A.J. Mannix, X.-F. Zhou, B. Kiraly, J.D. Wood, D. Alducin, B.D. Myers, X. Liu, B. L. Fisher, U. Santiago, J.R. Guest, et al., Synthesis of borophenes: anisotropic, two-dimensional boron polymorphs, *Science* 350 (6267) (2015) 1513–1516.

- [23] B. Feng, J. Zhang, Q. Zhong, W. Li, S. Li, H. Li, P. Cheng, S. Meng, L. Chen, K. Wu, Experimental realization of two-dimensional boron sheets, *Nat. Chem.* 8 (6) (2016) 563–568.
- [24] Q. Weng, D.G. Kvashnin, X. Wang, O. Cretu, Y. Yang, M. Zhou, C. Zhang, D.-M. Tang, P.B. Sorokin, Y. Bando, et al., Tuning of the optical, electronic, and magnetic properties of boron nitride nanosheets with oxygen doping and functionalization, *Adv. Mater.* 29 (28) (2017) 1700695.
- [25] C. Zhi, Y. Bando, C. Tang, D. Golberg, Boron nitride nanotubes, *Mater. Sci. Eng.* 70 (3–6) (2010) 92–111.
- [26] R. Han, F. Liu, X. Wang, M. Huang, W. Li, Y. Yamauchi, X. Sun, Z. Huang, Functionalised hexagonal boron nitride for energy conversion and storage, *J. Mater. Chem. A* 8 (29) (2020) 14384–14399.
- [27] W. Lei, S. Qin, D. Liu, D. Portehault, Z. Liu, Y. Chen, Large scale boron carbon nitride nanosheets with enhanced lithium storage capabilities, *Chem. Commun.* 49 (4) (2013) 352–354.
- [28] C. Huang, C. Chen, M. Zhang, L. Lin, X. Ye, S. Lin, M. Antonietti, X. Wang, Carbon-doped bn nanosheets for metal-free photoredox catalysis, *Nat. Commun.* 6 (1) (2015) 1–7.
- [29] J. Dai, X. Wu, J. Yang, X.C. Zeng, Unusual metallic microporous boron nitride networks, *J. Phys. Chem. Lett.* 4 (20) (2013) 3484–3488.
- [30] S. Zhang, Q. Wang, Y. Kawazoe, P. Jena, Three-dimensional metallic boron nitride, *J. Am. Chem. Soc.* 135 (48) (2013) 18216–18221.
- [31] M. Xiong, Z. Gao, K. Luo, F. Ling, Y. Gao, C. Chen, D. Yu, Z. Zhao, S. Wei, Three metallic bn polymorphs: 1d multi-threaded conduction in a 3d network, *PCCP* 22 (2) (2020) 489–496.
- [32] M. Wu, X. Wu, Y. Pei, Y. Wang, X.C. Zeng, Three-dimensional network model of carbon containing only sp²-carbon bonds and boron nitride analogues, *Chem. Commun.* 47 (15) (2011) 4406–4408.
- [33] S. Hao, G. Zhou, W. Duan, J. Wu, B.-L. Gu, Transverse pressure induced phase transitions in boron nitride nanotube bundles and the lightest boron nitride crystal, *J. Am. Chem. Soc.* 130 (15) (2008) 5257–5261.
- [34] M.M. Obeid, Q. Sun, Assembling biphenylene into 3d porous metallic carbon allotrope for promising anode of lithium-ion batteries, *Carbon N Y* 188 (2022) 95–103.
- [35] J. Ye, A.C. Baumgaertel, Y.M. Wang, J. Biener, M.M. Biener, Structural optimization of 3d porous electrodes for high-rate performance lithium ion batteries, *ACS Nano* 9 (2) (2015) 2194–2202.
- [36] Q. Zhao, Q. Zhu, J. Miao, P. Zhang, P. Wan, L. He, B. Xu, Flexible 3d porous mxene foam for high-performance lithium-ion batteries, *Small* 15 (51) (2019) 1904293.
- [37] Z. Fang, Q. Xing, D. Fernandez, X. Zhang, G. Yu, A mini review on two-dimensional nanomaterial assembly, *Nano Res.* 13 (5) (2020) 1179–1190.
- [38] I. Muhammad, U. Younis, H. Xie, A.A. Khan, A. Khaliq, A. Samad, U. Schwingenschlöggl, Q. Sun, Borophene-based three-dimensional porous structures as anode materials for alkali metal-ion batteries with ultrahigh capacity, *Chem. Mater.* 33 (8) (2021) 2976–2983.
- [39] J. Dai, X. Wu, J. Yang, X.C. Zeng, Porous boron nitride with tunable pore size, *J. Phys. Chem. Lett.* 5 (2) (2014) 393–398.
- [40] G. Kresse, J. Furthmüller, Efficient iterative schemes for ab initio total-energy calculations using a plane-wave basis set, *Phys. Rev. B* 54 (16) (1996) 11169.
- [41] J.P. Perdew, K. Burke, M. Ernzerhof, Generalized gradient approximation made simple, *Phys. Rev. Lett.* 77 (18) (1996) 3865.
- [42] P.E. Blöchl, Projector augmented-wave method, *Phys. Rev. B* 50 (24) (1994) 17953.
- [43] H.J. Monkhorst, J.D. Pack, Special points for brillouin-zone integrations, *Phys. Rev. B* 13 (12) (1976) 5188.
- [44] G. Henkelman, A. Arnaldsson, H. Jónsson, A fast and robust algorithm for bader decomposition of charge density, *Comput. Mater. Sci* 36 (3) (2006) 354–360.
- [45] G. Henkelman, B.P. Uberuaga, H. Jónsson, A climbing image nudged elastic band method for finding saddle points and minimum energy paths, *J. Chem. Phys.* 113 (22) (2000) 9901–9904.
- [46] S. Maintz, V.L. Deringer, A.L. Tchougréff, R. Dronskowski, Lobster: a tool to extract chemical bonding from plane-wave based dft, *J. Comput. Chem* 37 (11) (2016) 1030–1035.
- [47] F. Mouhat, F.-X. Coudert, Necessary and sufficient elastic stability conditions in various crystal systems, *Phys. Rev. B* 90 (22) (2014) 224104.
- [48] D. Chung, W. Buessem, The voigt-reuss-hill approximation and elastic moduli of polycrystalline mgo, caf₂, β -zns, znse, and cdte, *J. Appl. Phys.* 38 (6) (1967) 2535–2540.
- [49] S. Pugh, Xcii. relations between the elastic moduli and the plastic properties of polycrystalline pure metals, *Lond. Edinbur. Dubl. Philosoph. Mag. J. Sci.* 45 (367) (1954) 823–843.
- [50] D. Singh, R. Ahuja, Theoretical prediction of a bi-doped β -antimonene monolayer as a highly efficient photocatalyst for oxygen reduction and overall water splitting, *ACS Appl. Mater. Interface.* 13 (47) (2021) 56254–56264.
- [51] G.K. Madsen, D.J. Singh, Boltztrap. a code for calculating band-structure dependent quantities, *Comput. Phys. Commun.* 175 (1) (2006) 67–71.
- [52] U. Younis, I. Muhammad, W. Wu, S. Ahmed, Q. Sun, P. Jena, Assembling si 2 bn nanoribbons into a 3d porous structure as a universal anode material for both li- and na-ion batteries with high performance, *Nanoscale* 12 (37) (2020) 19367–19374.
- [53] Y. Qie, J. Liu, S. Wang, Q. Sun, P. Jena, Tetragonal c 24: a topological nodal-surface semimetal with potential as an anode material for sodium ion batteries, *J. Mater. Chem. A* 7 (10) (2019) 5733–5739.
- [54] Z. Wang, A.P. Ratvik, T. Grande, S.M. Selbach, Diffusion of alkali metals in the first stage graphite intercalation compounds by vdW-dft calculations, *RSC Adv.* 5 (21) (2015) 15985–15992.
- [55] P. Ge, M. Foulletier, Electrochemical intercalation of sodium in graphite, *Solid State Ion.* 28 (1988) 1172–1175.
- [56] J. Sun, M. Sadd, P. Edenborg, H. Grönbeck, P.H. Thiesen, Z. Xia, V. Quintano, R. Qiu, A. Matic, V. Palermo, Real-time imaging of na⁺ reversible intercalation in “janus” graphene stacks for battery applications, *Sci Adv* 7 (22) (2021) eabf0812.
- [57] H. Huang, H.-H. Wu, C. Chi, J. Zhu, B. Huang, T.-Y. Zhang, Out-of-plane ion transport makes nitrogenated holey graphite a promising high-rate anode for both li and na ion batteries, *Nanoscale* 11 (40) (2019) 18758–18768.
- [58] J. Liu, S. Wang, Q. Sun, All-carbon-based porous topological semimetal for li-ion battery anode material, *Proceed. Natl. Acad. Sci.* 114 (4) (2017) 651–656.
- [59] H. Xie, Y. Qie, M. Imran, Q. Sun, Topological semimetal porous carbon as a high-performance anode for li-ion batteries, *J. Mater. Chem. A* 7 (23) (2019) 14253–14259.
- [60] U. Younis, I. Muhammad, F. Qayyum, Y. Kawazoe, Q. Sun, A stable metallic 3d porous bpc 2 as a universal anode material for li, na, and k ion batteries with high performance, *Journal of Materials Chemistry A* 8 (48) (2020) 25824–25830.
- [61] Y. Qie, S. Wang, Q. Sun, Three dimensional metallic porous sic₄ allotropes: stability and battery applications, *Nano Energy* 63 (2019) 103862.
- [62] A. Samad, A. Shafique, Y.-H. Shin, Adsorption and diffusion of mono, di, and trivalent ions on two-dimensional tis₂, *Nanotechnology* 28 (17) (2017) 175401.
- [63] N. Khossossi, A. Banerjee, I. Essaoudi, A. Ainane, P. Jena, R. Ahuja, Thermodynamics and kinetics of 2d g-gec monolayer as an anode materials for li/na-ion batteries, *J. Power Source.* 485 (2021) 229318.
- [64] K. Persson, Y. Hinuma, Y.S. Meng, A. Van der Ven, G. Ceder, Thermodynamic and kinetic properties of the li-graphite system from first-principles calculations, *Phys. Rev. B* 82 (12) (2010) 125416.
- [65] Y.-F. Deng, S.-X. Zhao, Y.-H. Xu, K. Gao, C.-W. Nan, Impact of p-doped in spinel lini_{0.5}mn_{1.5}o₄ on degree of disorder, grain morphology, and electrochemical performance, *Chem. Mater.* 27 (22) (2015) 7734–7742.